# Local thermal conductivity of polycrystalline AlN ceramics measured by scanning thermal microscopy and complementary scanning electron microscopy techniques*

Zhang Yue-Fei(张跃飞)[a)], Wang Li(王 丽)[a)], R. Heiderhoff[b)], A. K. Geinzer[b)], Wei Bin(卫 斌)[a)], Ji Yuan(吉 元)[a)], Han Xiao-Dong(韩晓东)[a)†], L. J. Balk[b)], and Zhang Ze(张 泽)[a)c)]

[a)] *Institute of Microstructure and Property of Advanced Materials, Beijing University of Technology, Beijing* 100124, *China*

[b)] *Department of Electronics, Faculty of Electrical, Information and Media Engineering, University of Wuppertal, Wuppertal D-*42119, *Germany*

[c)] *Department of Materials Science, Zhejiang University, Hangzhou* 300038, *China*

(Received 11 March 2011; revised manuscript received 26 July 2011)

The local thermal conductivity of polycrystalline aluminum nitride (AlN) ceramics is measured and imaged by using a scanning thermal microscope (SThM) and complementary scanning electron microscope (SEM) based techniques at room temperature. The quantitative thermal conductivity for the AlN sample is gained by using a SThM with a spatial resolution of sub-micrometer scale through using the $3\omega$ method. A thermal conductivity of 308 W/m·K within grains corresponding to that of high-purity single crystal AlN is obtained. The slight differences in thermal conduction between the adjacent grains are found to result from crystallographic misorientations, as demonstrated in the electron backscattered diffraction. A much lower thermal conductivity at the grain boundary is due to impurities and defects enriched in these sites, as indicated by energy dispersive X-ray spectroscopy.

**Keywords:** thermal conductivity, AlN ceramics, scanning thermal microscopy, scanning electron microscopy

**PACS:** 65.40.–b, 66.70.Df **DOI:** 10.1088/1674-1056/21/1/016501

## 1. Introduction

Aluminum nitride (AlN) ceramics possess outstanding properties, including good thermal stability, high thermal conductivity, low coefficient of thermal expansion, high dielectric constant, and so on.[1,2] These properties make AlN suitable for electronic and optoelectronic devices.[3,4] For the practical application of polycrystalline AlN in miniaturized electronic devices, it is important to investigate its local thermal conductivity at the submicron scale. The microstructures of polycrystalline ceramics, including grain sizes, crystallographic orientations, grain boundary types, compositions, impurities, and defects, not only influence the total thermal property, but also induce differences in local heat dissipation. For example, the thermal conductivity of a pure single crystal AlN is predicted to be 320 W/m·K at room temperature, while that of a sintering polycrystalline AlN is reduced into a range between 100 W/m·K and 260 W/m·K.[5]

Local thermal measurement with a high spatial resolution can provide the missing link for understanding the relationship between the thermal conduction mechanism and the microstructure.[6] The scanning thermal microscope (SThM) is a powerful tool for measuring the thermal conductivity and the temperature distribution with a high spatial resolution of about 30 nm.[7,8] The $3\omega$ method allows quantitative measurement of the thermal conductivities of low and high thermal conducting materials with an excellent spatial resolution and a high accuracy.[9] The local thermal conductivities through grains, grain

*Project supported by the National Basic Research Program of China (Grant No. 2009CB623702), the National Natural Science Foundation of China (Grant No. 10904001), and the Key Project Funding Scheme of Beijing Municipal Education Committee, China (Grant No. KZ201010005002).

†Corresponding author. E-mail: xdhan@bjut.edu.cn

© 2012 Chinese Physical Society and IOP Publishing Ltd

boundaries, interfaces, and layered structures can be measured simultaneously with the topography by using the SThM. Complementary investigations can be performed at the same position by using a scanning electron microscope (SEM) or an environmental SEM (ESEM) as well as some other (E)SEM based techniques such as electron backscattered diffraction (EBSD) and energy dispersive X-ray spectroscopy (EDS). An advantage of using the ESEM under low vacuum conditions is the compensation of the electrical charge effect during the electron irradiation on the nonconductive sample. An (E)SEM equipped with the EBSD and the EDS can achieve the crystallographic orientation measurement, the phase identification, and the elemental analysis simultaneously.

In this work, an SThM with the frequency dependent $3\omega$ method is used for the thermal imaging and the quantitative measurement of the thermal conductivities across the grains and the grain boundaries on polycrystalline AlN samples at room temperature.[10] The influences of grain orientations, grain boundary characteristics, and impurity distributions on the thermal conductivity are analysed by using these complementary SEM techniques.

## 2. Experiment

A polycrystalline AlN sample was synthesized by using 95 wt.% AlN powder with 5 wt.% $Y_2O_3$ powder as the sintering aid. They were mixed with high purity acetone in a ball mill. The slurry was dried in a vacuum oven and then sintered by spark plasma sintering (SPS) at 1800 °C. The AlN sample with a thickness of approximately 2 mm was annealed at 1100 °C to eliminate the surface stress. To avoid rough artefacts in the SThM and (E)SEM experiments, the surface of the AlN sample was well polished.

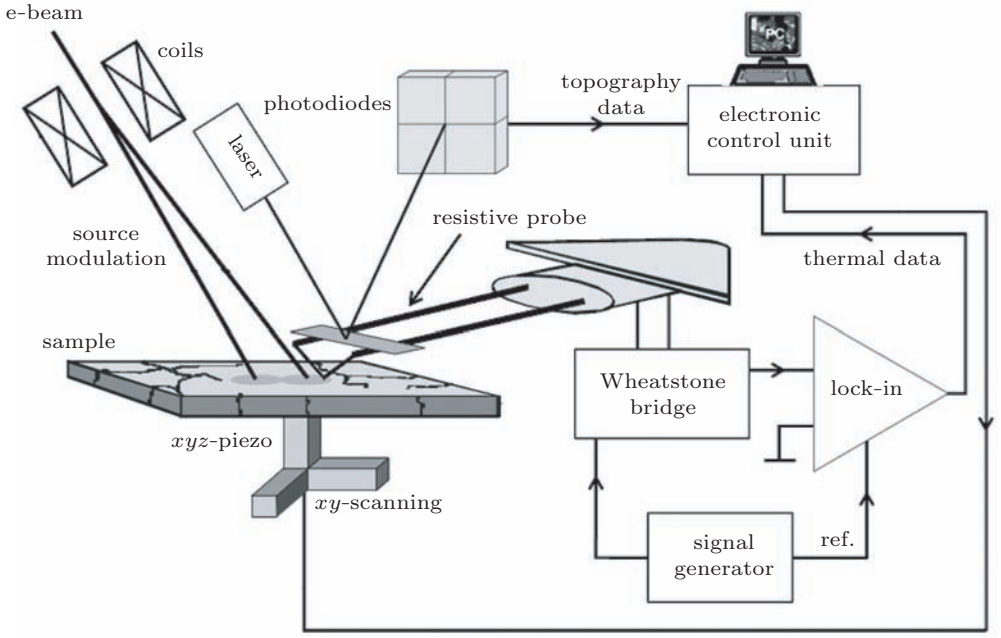



**Fig. 1.** Schematic set-up of the SThM–ESEM hybrid system.

A scanning thermal microscope was incorporated into the chamber of the environmental scanning electron microscope (ESEM, FEI Quanta 200) to perform the complementary microscopy techniques at the same sample position, as illustrated in Fig. 1. This SThM–ESEM hybrid system also allowed us to measure the thermal transport at the interfaces using an electron beam induced heat source, which has been described elsewhere.[9] The operating parameters of the ESEM involved a primary electron energy of 20 keV, a primary current of $\sim 7\times10^{-11}$ A, a scan rate of 80 s per frame, and a vacuum range of 30–80 Pa. A resistive SThM thermal probe was placed at the end of the scanning probe microscope (SPM) cantilever to carry out the thermal conductivity measurement. The probe acted both as a heater that induced a thermal

wave into the sample and as a thermometer to detect the material-dependent resistance variation of the thermal probe.[11] The resistive probe was integrated into the alternating current (AC) based Wheatstone bridge to measure the resistance changes. A frequency triple multiplier of the signal frequency ($3\omega$) served as the reference of the lock-in amplifier. As the heat flow varied across regions of different thermal conductivities on the AlN sample during the scan, the resistance of the probe tip changed and unbalanced the Wheatstone bridge. The output voltage of the bridge was fed into the lock-in amplifier to detect the resistance change with the highest sensitivity and to acquire the thermal image. Thermal and topographic data were simultaneously obtained by using the resistive probe and were recorded by an electronic control unit and a PC. The SThM with the $3\omega$ method for measuring quantitatively thermal conductivity $\lambda$ has been demonstrated by Altes *et al.*[12,13]

Moreover, a thermal field emission SEM (JEOL 6500F) with an EBSD-EDS system (EDAX-TSL) was used for the crystallographic microstructure analysis with a primary electron energy of 15 keV to reach a high lateral resolution.

## 3. Results and discussion

The thermal image obtained with the $3\omega$ method at an applied heating frequency $\omega$ of 660 Hz and the matched topographic image of the polycrystalline AlN sample are shown in Figs. 2(a) and 2(b), respectively. The adjacent grains exhibit different contrasts in the thermal image. The contrast between the grains appears dark and bright, corresponding to the lower and the higher thermal conductivities, respectively. Furthermore, the grain boundaries can clearly be distinguished in the thermal and the topographic images, suggesting that the frequency dependent thermal image has a high spatial resolution (about several tens of nanometers).

For a better understanding of the local thermal conductivity distribution, the analyses based on the thermal and the matched topographic images are shown in Fig. 3. Lines $A$ and $A'$ cross over a wide grain boundary (denoted as 1 and 1′), while lines B and B′ cross over two narrow grain boundaries (denoted as 2 and 2′, 3 and 3′) and a grain (denoted as 4 and 4′). The thermal profiles along lines $A$ and $B$ in the thermal image are shown in Figs. 3(b) and 3(c), respectively, while the topographic profiles along lines $A'$ and $B'$ in the topographic image are shown in Figs. 3(e) and 3(f), respectively. The thermal and the matched topographic profiles clearly indicate the differences in the local thermal conductivity. From the images, we notice the following properties. (i) The highest $\lambda$ is located within the grain (denoted as 4 and 4′). (ii) The difference in thermal conductivity between the neighbouring grains is smaller than that between the grain and the grain boundary. (iii) The wide grain boundary site (denoted as 1 and 1′) has the lowest value of the output voltage, indicated by the lowest site of the thermal conductivity. (iv) With the SThM, a spatial resolution of about 100 nm can be achieved, as determined from the topographic profile shown in Fig. 3(f).

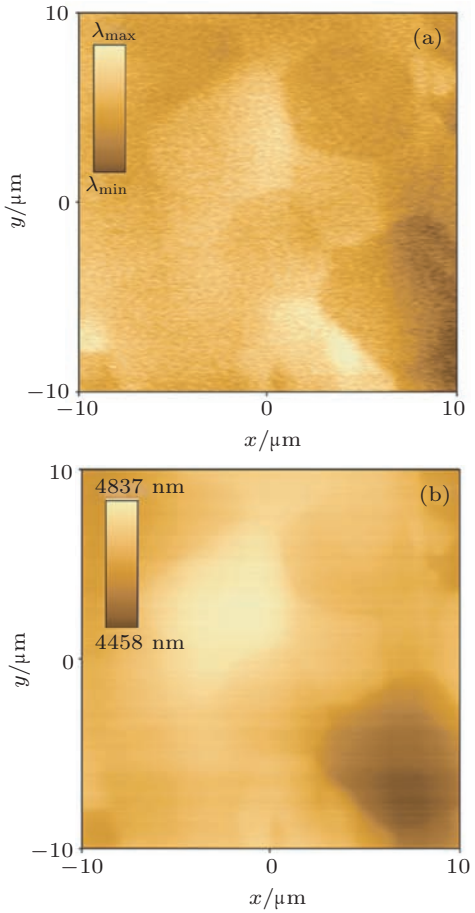



**Fig. 2.** (colour online) Thermal (a) and topographic (b) images of AlN sample obtained with the SThM–ESEM hybrid system.

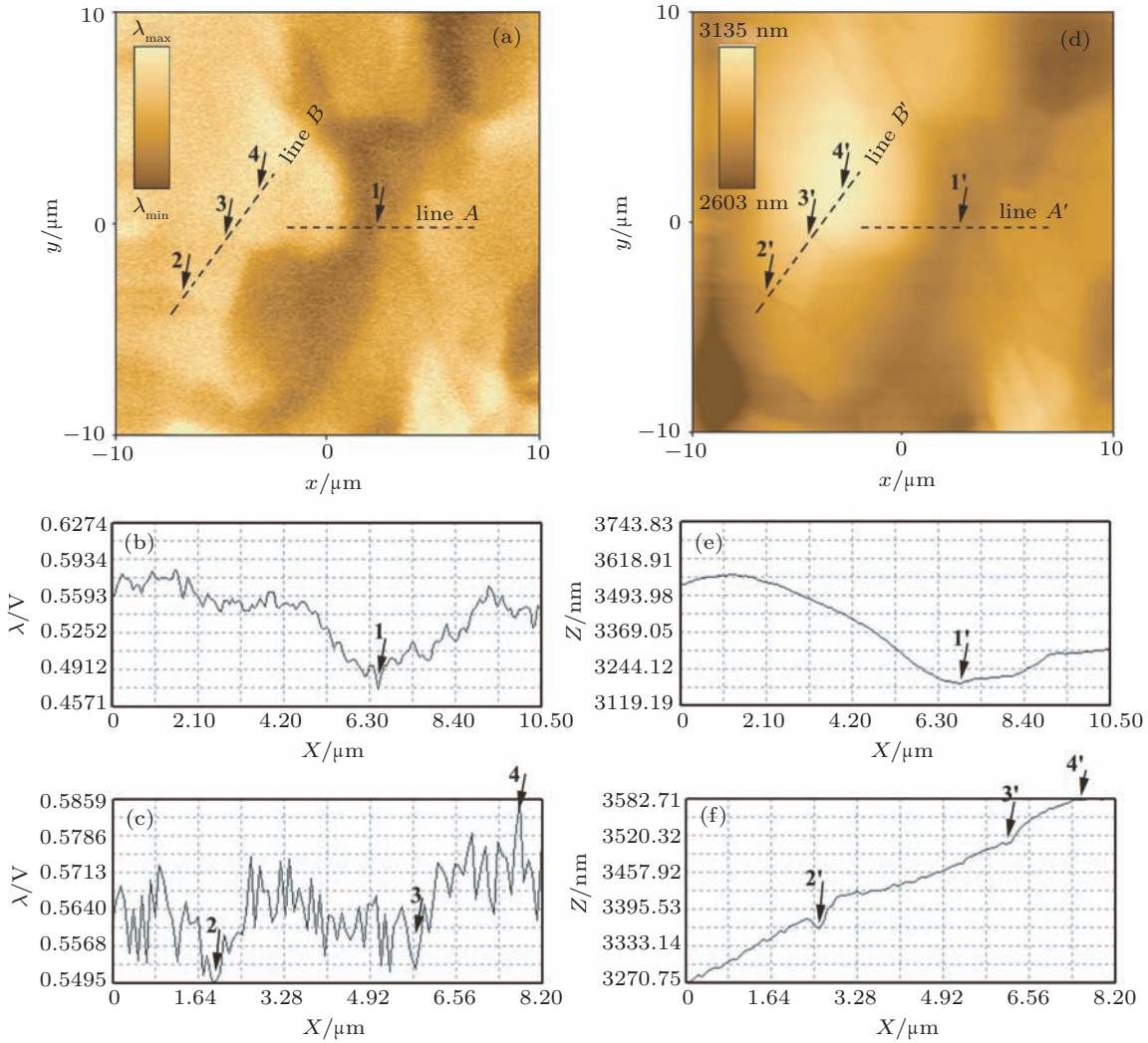



**Fig. 3.** (colour online) SThM line measurements of the AlN sample: (a) thermal image with lines $A$ and $B$, (b) and (c) corresponding thermal profiles along lines $A$ and $B$, (d) matched topographic image with lines $A'$ and $B'$, (e) and (f) corresponding topographic profiles along lines $A'$ and $B'$.

Thermal conductivity $\lambda$ within the grain and at the grain boundary on the AlN sample is quantitatively measured by the SThM using the spectral response of the $3\omega$ signal.[13] We have

$$U_{3\omega 1} - U_{3\omega 2} = \frac{1}{4} I_0 \frac{\mathrm{d}R}{\mathrm{d}T} \frac{P}{l\pi\lambda} [\ln(\omega_1) - \ln(\omega_2)], \quad (1)$$

where $U_{3\omega 1}$ and $U_{3\omega 2}$ are the output voltages of the Wheatstone bridge at two angular frequencies of the $3\omega$ component, $I_0$ is the current passing through the resistive probe (heater), $\mathrm{d}R/\mathrm{d}T$ is the temperature coefficient of the probe, for which the reference value is 0.00165 $\mathrm{K}^{-1}$ (Vecco), and $P$ is the amplitude of the power per unit length. The value of $\lambda$ is determined by the angular frequency of the resistive probe ($\omega$) versus the output voltage ($3\omega$) of the Wheatstone bridge curves (Eq. (1)) at room temperature. Figure 4 shows the heater frequency ($\omega$)–output voltage ($3\omega$) curves of a pure gold film (as the reference material)[7,14] and $\omega$ the AlN sample. The curves for the AlN sample are obtained at the grain boundary and within the grain centre (site 1 of line A and site 4 of line B in Fig. 3(a)). Note that the heater frequency ($\omega$)–output voltage ($3\omega$) curve of the gold film is obtained assuming the thermal conductivity of the pure gold film to be 318 W/m·K. The value of the thermal conductivity at each point in the thermal image is assigned by calculating the slope $1/\lambda$ of the curve. The $\lambda$ values of a grain boundary and within a grain in the thermal image (sites 1 and 4) are given to be 288 W/m·K and 308 W/m·K, respectively. The measured results indicate that $\lambda$ within a grain is close to that of the high-purity single crystal AlN (320 W/m·K), while $\lambda$ obviously reduces at the grain boundary. In principle, only two different angular frequencies are necessary

for determining the slope of the $\omega$–$3\omega$ curve. Measurements at more frequencies (here 21 different frequencies) allow for the improvement of measurement accuracy and the calibration of the frequency dependence of the data acquirement system.

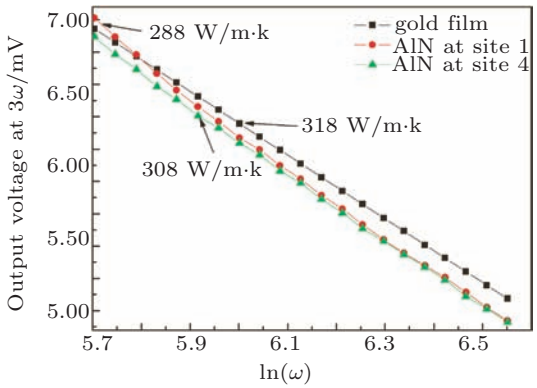



**Fig. 4.** (colour online) Heater frequency ($\omega$)–output voltage ($3\omega$) curves of thermal conductivity measurements for AlN sample and gold film.

These differences in the local thermal conductivity of the AlN sample are due to the polycrystalline microstructures, including the grain size, the crystallographic orientation, the grain boundary type, and the impurity distribution, which are demonstrated by the EBSD measurement and the EDS analysis. Figure 5(a) shows the backscattered electron (BSE) image. The grain size is several tens of micrometers in diameter, as shown in the BSE image, consisting of that shown in the SThM images (Fig. 2). Note that the image contrast of the BSE for the polycrystalline AlN sample clearly displays grain orientations (channelling contrast) and secondary phase distributions (material contrast). Figure 5(b) shows the crystallographic orientation map with a high angle boundary ($\geq 15°$) obtained by the EBSD, which clearly exhibits the random orientation distribution of the AlN grains. The BSE and the EBSD results suggest that the slight differences in thermal conduction between the neighbouring grains result from the grain misorientations.

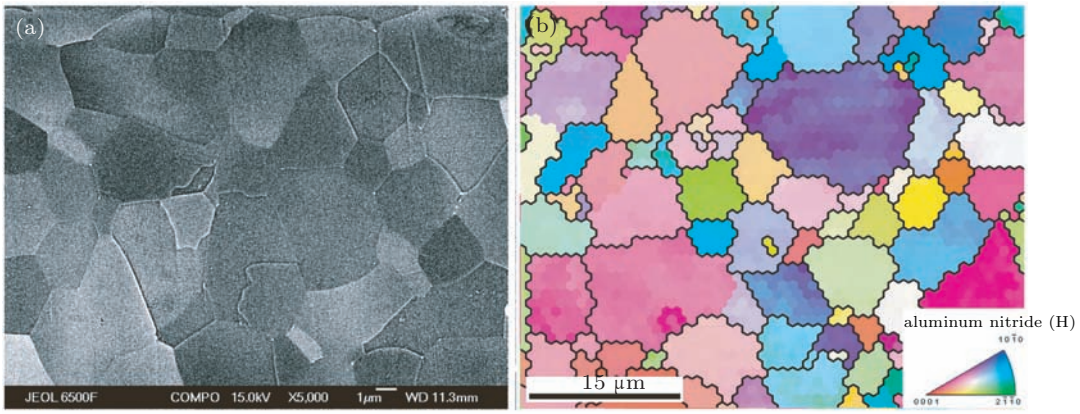



**Fig. 5.** (colour online) (a) BSE image and (b) grain orientation map with a high angle boundary distribution ($\geq 15°$) for AlN sample.

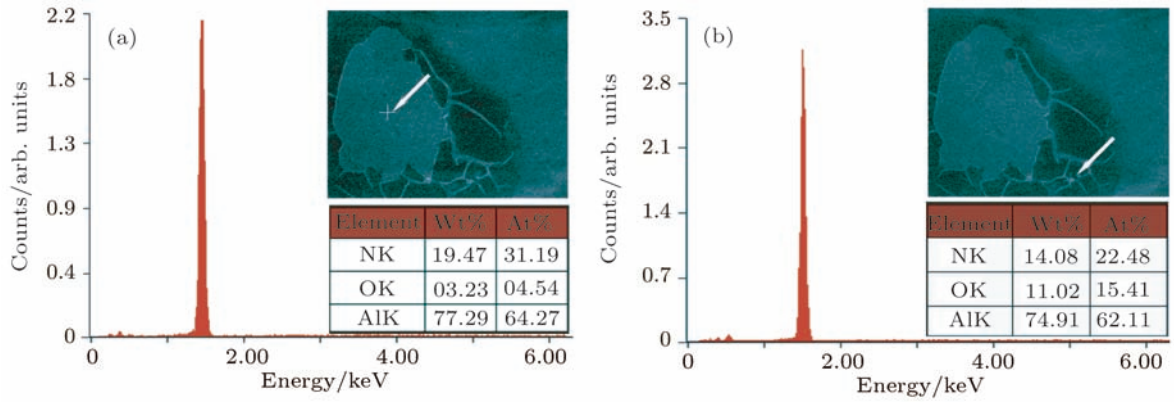



**Fig. 6.** (colour online) Element analyses obtained by the EDS for the AlN sample (a) within a grain (b) and at the grain boundary shown by the white arrows.

The EDS analysis for the AlN sample indicates the oxygen element to be 3.14–3.23 wt.% within the grains whereas 5.13–11.02 wt.% at the boundaries as shown in Figs. 6(a) and 6(b), respectively. These results suggest that the additive $Y_2O_3$ as the secondary phase in the AlN ceramics is mostly distributed at the grain boundary. Oxygen and yttrium elements enriched along the grain boundaries are also clearly indicated by the brighter spot contrast in the BSE image, as shown in Fig. 5(a). These results indicate that the crystallographic orientations, the impurities, and the defect distributions each play a significant role in affecting the local thermal conductivity of the polycrystalline materials. The bright/dark contrast of the grains appearing in the thermal images (Figs. 2(a) and 3(a)) is mainly contributed by disorientated grains. The impurities and the defects may result in the increase of phonon–defect scattering or phonon–grain scattering.[15,16] These scattering processes lead to a decrease in the total and local thermal conductivities of the polycrystalline AlN ceramics.

# 4. Conclusion

Quantitative thermal conductivity imaging with a high special resolution is obtained for polycrystalline AlN ceramics by using scanning thermal microscopy (SThM) with the $3\omega$ method. A higher $\lambda$ value (308 W/m·K) within the grain is found, which corresponds to that of the high-purity single crystal AlN at the room temperature. The lower $\lambda$ value at the grain boundary is found to be 288 W/m·K.

The influences of the microstructures, including the grain orientation, the grain boundary features, and the oxygen distributions, on the local thermal conductivity of the AlN sample are analysed by using complementary SEM techniques, including the backscattered electron image, the EBSD crystallographic orientation map, and the EDS elemental analysis. The slight difference in thermal conduction between the adjacent grains is found to result from crystallographic misorientations. The obvious decrease in the thermal conduction at the grain boundary sites is due to the concentrations of impurities and defects at these sites.

It is demonstrated that for a better understanding of the thermal conduction mechanism at room temperature correlated to the crystallographic microstructures in polycrystalline materials, complementary SThM and SEM are promising techniques.

# Acknowledgment

The authors would like to thank Professor Li Yong-Li for providing the AlN samples.

# References

[1] AlShaikhi A and Srivastava G P 2008 *J. Appl. Phys.* **103** 083554

[2] Slack G A, Tanzilli R A, Pohl R O and Vandersande J W 1987 *J. Phys. Chem. Solids* **48** 641

[3] Medraj M, Baik Y, Thompson W T and Drew R A L 2005 *J. Mater. Proc. Technol.* **161** 415

[4] Franco J A and Shanafield D J 2004 *Ceramica* **50** 247

[5] AlShaikhi A and Srivastava G P 2009 *J. Phys.*: *Condens. Matter* **21** 174207

[6] Wang Z L, Tang D W, Jia T and Mao A M 2007 *Acta Phys. Sin.* **56** 747 (in Chinese)

[7] Fenwick O, Bozec L, Credgington D, Hammiche A, Lazzerini G M, Silberberg Y R and Cacialli F 2009 *Nat. Nanotechnol.* **4** 664

[8] Zhang Y F, Wang L, Ji Y, Han X D, Zhang Z, Heiderhoff R, Tiedemann A K and Balk L J 2009 *IEEE Proceedings of 16th IPFA* **CFP09777-CDR** 520

[9] Tiedemann A K, Heiderhoff R, Balk L J and Phang J C H 2009 *IEEE Proceedings of 16th IPFA* **CFP09RPS-CDR** 327

[10] Feng P and Wang T H 2003 *Acta Phys. Sin.* **52** 2249 (in Chinese)

[11] Joachimsthaler I, Heiderhoff R and Balk L J 2003 *Meas. Sci. Tech.* **14** 87

[12] Fiege G B M, Altes A, Heiderhoff R and Balk L J 1999 *J. Phys.* D: *Appl. Phys.* **32** 13

[13] Altes A, Heiderhoff R and Balk L J 2004 *J. Phys.* D: *Appl. Phys.* **37** 952

[14] Cahill D G 1990 *Rev. Sci. Instrum.* **61** 802

[15] Watari K, Nakano H, Urabe K, Ishizaki K, Cao S and Mori K 2002 *J. Mater. Res.* **17** 2940

[16] Lee S K, Yamda I, Kume S, Nakano H, Hatori K, Matsui G and Watari K 2008 *J. Ceram. Soc. Jap.* **116** 1260